Nanoscale

Accepted Manuscript

ROYAL SOCIETY OF CHEMISTRY

rsc.li/nanoscale

ARTICLE

ZIF-8 derived hollow carbon to trap polysulfides for high performance lithium-sulfur batteries.

Masud Rana[a,b,j,k], Jeonghum Kim[a,b] Lingyi Peng[c], Qiu He[d], Rejaul Kaiser[e], Lingbing Ran[f], Md. Shahriar A. Hossain[a,b], Bin Luo[a]*, Ian Gentle[g], Lianzhou Wang[a,i], Ruth Knibbe[b]* and Yusuke Yamauchi[a,h,i]*

Lithium-sulfur batteries (LSBs) have been considered very promising due to their high theoretical energy density and low cost. However, the undesirable shuttle effect with solid discharge product Li_2S, greatly impedes its market penetration. Functional elements associated conductive carbon materials are beneficial to control the shuttle effect and reactivate the Li_2S leading to long term cycling performance of LSBs. Herein, we report Zinc (Zn) and Nitrogen (N) associated ZIF-8 derived hollow carbon (ZHC) as a promising separator coating for LSBs to control the shuttle effect of LSBs. The hollow area in the ZHC is identified to be around 100 nm with a carbonized outer surface thickness of approximately 50 nm. The presence of Zn and N in the nano hollow structure of the carbon helps to mitigate the PS diffusion in LSBs. The hollow interior of the carbon acts as PS pocket to physically capture the PS and in addition Zn and N chemically attract the PS through polar-polar and metal sulfide interactions to further diffuse from cathode to anode during charging and discharging. The ZHC with its unique architecture and functional groups has been very promising to enable initial specific capacity (S.cap) of 842 mAh g^{-1} at 4.80 mg cm^{-2} and long run till 400 cycles, which is considerably higher in comparison to the cycling performance of parent ZIF-8.

Keywords: Shuttle effect, Li_2S reactivation, hollow architecture, chemical interactions.

a. Australian Institute for Bioengineering and Nanotechnology (AIBN), The University of Queensland QLD 4072, Australia

b. School of Mechanical and Mining Engineering, The University of Queensland, St Lucia, QLD 4072, Australia

c. Department of Chemical and Biomolecular Engineering, Yonsei University-50 Yonsei-ro seodaemun-gu,seol,120-749,Republic of Korea.

d. School of Chemical Engineering, The University of New South Wales, Sydney, NSW 2052, Australia

e. State School Key Laboratory of Silicate Materials for Architectures, International School of Materials Science and Engineering, Wuhan University of Technology, Wuhan 430070, Hubei, China.

f. Commonwealth Scientific and Industrial Research Organization (CSIRO), Manufacturing Business Unit, P.O. Box 218, Bradfield Road, Lindfield, NSW 2070, Australia

g. School of Chemistry and Molecular Biosciences, Faculty of Science, The University of Queensland, St Lucia, QLD 4072, Australia

h. JST-ERATO Yamauchi Materials Space-Tectonics Project and International Center for Materials Nanoarchitechtonics (WPI-MANA), National Institute for Materials Science (NIMS), 1-1 Namiki, Tsukuba, Ibaraki 305-0044, Japan†

i. School of Chemical Engineering, The University of Queensland QLD 4072, Australia

j. Research Scientist , Redflow International Pty Ltd, 27 Counihan Rd, Seventeen Mile Rocks QLD 4073

k. Industry Fellow, School of Chemistry and Molecular Biosciences, The University of Queensland, St Lucia, QLD 4072, Australia

Footnotes relating to the title and/or authors should appear here.
Electronic Supplementary Information (ESI) available: [details of any supplementary information available should be included here]. See DOI: 10.1039/x0xx00000x

Introduction

Commercial lithium-ion batteries has played a vital role in energy storage over the past decade. However, the energy density of lithium-ion batteries (240 Wh kg^{-1}, Panasonic NCR18650B) falls behind the ever-growing demand of energy storage applications. [1] Hence, alternative energy storage systems with a high energy density and durability are needed to fulfil the demand for a wide range of applications in electric vehicles and portable electronic devices. Among various alternative energy storage systems, lithium-sulfur batteries (LSBs) are considered as the most regarded candidates because of their excellent theoretical high gravimetric energy density of 2600 Wh kg^{-1}, natural abundance, low cost and environmentally friendliness. [1, 2] In spite of these valuable properties, the LSBs have not been yet commercialized due to the shuttle effect [3] (diffusion of polysulfides Li_2S_x, where x = 4,6,8 between anode and cathode) and the formation of the insulating solid Li_2S

ARTICLE

Journal Name

product, which forms during discharge. During charging, the Li_2S is supposed to be oxidized to S_8, however, in practice this requires a highly-conductive host material to ensure the electron access to the solid Li_2S. Otherwise, the insoluble Li_2S phase passivates the Li metal anode and deteriorates the mechanical integrity of the sulfur cathode. For the shuttle effect, high-order polysulfides (Li_2S_x, x = 4,6,8) can diffuse through the porous Celgard PP separator and form a Li_2S passivation layer on the Li metal anode. This passivation layer is electronically and ionically insulating with a low Li^+ diffusivity of 10^{-15} cm^2 s^{-1}. [4] The shuttle effect coupled with the solid passivation layer formation leads to a continuous loss of active sulfur and degrades both electrodes. This eventually affects the coulombic efficiency, cycling stability and self-discharge of LSBs. Therefore, new materials need to be designed which can stop the diffusion of high-order PSs and reactivate the solid Li_2S in LSBs.

To address the aforementioned issues, non-polar carbon materials have been widely used in LSBs as sulfur host. However, these materials only interact with the polar PSs through weak van der Waals interactions and as such are only show a weak bonding (0.1-0.7 eV). [5] As such, the PSs tend to diffuse out of the carbon structure at room temperature. Also, the pore size of the carbon hosts is larger than the PS dimension (2 nm), providing no limited physical trapping effect. [6] Therefore, suitable host materials associated with functionally interactive elements and micropores ≤ 2nm, need to be designed to mitigate the shuttle issue of LSBs. [7] The functional materials with higher binding energies with PSs can be an effective way to chemically interact with the PSs through polar-polar and Lewis acid-base interactions. [8-11] Hollow porous carbon materials also have been widely used to physically confine the PSs into its assembly structure to the development of various LSBs. [12] Recent investigations has indicated that hollow carbon materials are suitable to improve the performance of LSBs. [13] Therefore, the appropriate design of hollow carbon with functional elements could be a promising pathway to promote the LSBs research.

For the first time, this research aims to design microporous ZHC materials associated with the Lewis acid Zn and electronegative N sites to coat the Celgard PP separator of LSBs to physically and chemically interact with the PSs. This material has been implemented to coat the Celgard PP separator. The typical Celgard PP separator has larger pores which are approximately a few hundred micrometres in size to allow for fast ion transport. Unfortunately, this large porosity also facilitates the PSs resulting loss of active materials in LSBs during cycling. The ZHC coating on top of

the Celgard PP suppresses the diffusion of PSs through Lewis acid and polar-polar interactions by chemically interactive Zn and N sites. Moreover, the microporous structure (≤ 2 nm) acts as a physical barrier to PSs (~ 2 nm). At the same time, the conductive scaffold of the ZHC promotes the electron access to the solid discharge PSs products to S_8. Benefiting from these advantages, the ZHC coated Celgard PP driven LSBs exhibits initial specific capacity (S.cap) of 842 mAh g^{-1} at 4.80 mg cm^{-2} and a long run up to 400 cycles. This is considerably higher in comparison to the parent ZIF-8 LSB.

Results and Discussion

Zeolitic imidazolate frameworks-8 (ZIF-8) was considered as a parent MOF for ZHC production which was synthesized by the chemical reactions of zinc acetate (Zn $(CH_3COO)_2 \cdot 2H_2O$) precursor and 2-methylimidazole ($C_4H_6N_2$) [14] **(Figure 1a)**. The monocrystalline MOF nanobubbles were produced through a controlled etching process of parent ZIF-8 in the presence of tanic acid, which is unlike the well-known conventional templating methods, Kirkendall effect, or Ostwald ripening. [15-19] Basically, after immersing the parent ZIF-8 nanocrystals in the tanic acid, the centre of the ZIF-8 MOF was sufficiently removed due to the diffusion of the protons in the assembly architecture of the parent ZIF-8. As a result, the core region was chemically etched with nanoscale precision and maintained the monocrystalline framework of the outer surface of the monocrystalline MOF nanobubbles **(Figure 1b)**. The monocrystalline MOF nanobubbles further pyrolyzed at 800 °C in the presence of Ar gas to convert into hollow nanoporous nanobubble carbon particles (**Figure 1c**). The carbonaceous nanobubbles possess a hollow interior structure which can encapsulate the PSs and allow easy access of electron and Li^+/Li ion intercalation (**Figure 1e**).
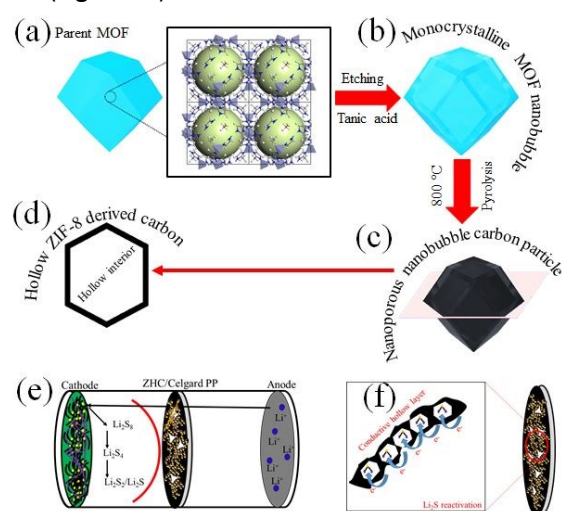
Figure 1. Schematic illustration of (a) parent MOF, (b) monocrystalline MOF nanobubble with hollow interior, (c & d) carbonized nanoporous nanobubble carbon particle with hollow interior. (e) conceptual schematic of LSBs in the presence of ZHC coated Celgard PP separator to block the PSs diffusion to andoe. (e) shows how the electrons are accessed to the solid Li₂S to be reactivated inside the hollow interior of ZHC.

Figure 1e is showing the conceptual diagram on how the ZHC coating defend the PSs diffusion in LSBs to further react with the anode. The hollow structure of ZHC with the encapsulated Li₂S inside its hollow region is shown in **Figure 1f**. The outer conductive layer of the ZHC is beneficial as it can reactivate the insulating solid Li₂S by providing easy access to electron and ion supply.

The scanning electron microscopy (SEM) and transmission electron microscopy (TEM) were used to investigate the surface morphology of the materials. **Figure S1a & b** presents the TEM images of the parent ZIF-8 MOF at low and high magnification, respectively. The ZIF-8 particles have a rhombic dodecahedral architecture with truncated corners and the particle size is approximately 1 μm. The morphology of the synthesized ZHC is presented in **Figure 2**. **Figure 2a** is a SEM image showing a uniform, well-dispersed morphology, which is obviously different from the bulk morphology of the agglomerated ZIF-8. The aggregation and agglomeration of the hollow nanoparticles can be due to the Brownian motion where nanoparticles collide and stick together because of their random, Brownian motion. Another mechanism that leads to the agglomeration of such nanoparticles is known as gravitational agglomeration, which is dependent on the size of the particles and their terminal velocity. The slowly settling particles are caught by the more rapidly settling particles, leading to the agglomeration.[20] The Celgard PP and ZHC coated Celgard PP is shown in **Figure S2a-b**. The ZHC maintain it morphology after coating on top of the Celgard PP separator. **Figure 2b & c** further present the TEM images at low and high magnification for ZHC. From the low magnification, the hollow structures in the ZHC is noticed to be around 100 nm with carbonized outer surface having a thickness of approximately 50 nm. Considering the maximum dimension of the PSs ~ 2 nm, [21] the speculation is at least 25 higher order PSs can be accommodated into this hollow structure of ZHC. Also, it is anticipated that these localized PSs will receive electron and Li⁺ ions and as such can be reactivated on the conductive, outer surface of the ZHC (**Figure 1e&f**). The elemental distribution of zinc, carbon, nitrogen and oxygen is presented in **Figure 2d-f** by the EDS mapping. The incomplete elimination of Zn in the

ZHC was intentional to get the Lewis acid base Zn in the ZHC structure. This is because; the complete elimination of Zn from the ZHC structure would improve the high surface area but would compromise the Lewis acidic Zn sites.The high surface area is crucial for LSBs to accommodate the PSs. On the other hand, the Zn and N presences in the hollow structure is crucial to attract the PSs through Lewis acid base and polar-polar interactions. Hence, considering these needful parameters the ZHC was treated by the tanic acid controllably to have the good surface area and presence of Zn to physically accommodate the PSs and chemically interact.[11] **Figure 2c** shows the high-resolution TEM image of the ZHC, where the structure is shown to be highly disorder structure indicating the conversion of the parent ZIF-8 into hollow carbon. The BET surface area of ZHC was confirmed to be 160 m²/g with a pore volume of 0.15 cm³/g and microporous nature **Figure S3**.

The crystallinity and phase purity of the parent ZIF-8 was identified in comparison with the ZHC by X-ray diffraction (XRD) (**Figure 3a**). The recorded XRD pattern of the parent ZIF-8 indicates a well-defined crystal structure [22] (**Figure 3a**). After pyrolysis of the ZIF-8 at 800° C, the ZHC becomes amorphous showing a broad peak centred at 26.3°, which is from the (002) graphitic planes of the parent ZIF-8. [23] This amorphous peak is also supported by the HRTEM image shown in **Figure 2c**.

The surface elements in ZHC were identified by X-ray photoelectron spectroscopy (XPS) as shown in **Figure 3b-f**. In the survey of the ZHC, Zn 2p, F 1s, O 1s, N 1s and C 1s were traced as 0.37, 0.53, 3.39, 91.22 and 3.68 %, respectively (**Figure 3b**). The higher atomic concentration of carbon and the C-C peak at 284.6 eV is indicating that the parent ZIF-8 is successfully converted into ZHC. Also, in the high-resolution peak of carbon, the C-C peak at 284.6 eV is indicating the successful conversion of crystal ZIF-8 into ZHC. In addition, the presence of Zn metal and electronegative N in the carbon structure is beneficial to enable Lewis acid and polar-polar interactive sites to chemically interact with the PS. [8, 24, 25] In the high-resolution peak of N1s, the detected three different peaks are indicated as pyridinic, pyrrolic and graphitic N at 399.1, 400.0 and 401.0 eV, respectively. The dominant presence of the pyridinic group is significant in forming the chemical interactions with PSs anion as SxLi···N by the lone pair electron of N. [26] The high-resolution scan of the Zn 2p spectra is shown in **Figure 3f,** where the presence of Zn 2p₃/₂ is confirmed at 1021.2 eV. The Zn should act as a Lewis acid site for PS chemisorption. Also, the carbon structure the presence of Zn-O is shown in Figure 3e.
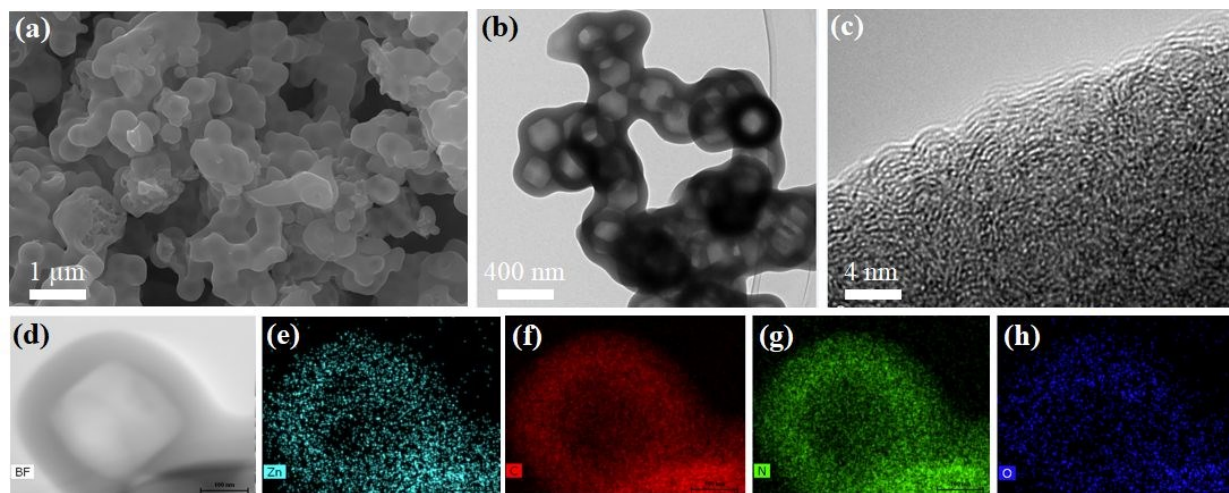
Figure 2. (a) SEM image of ZHC. (b) low magnified TEM image of ZHC is showing hollow interior architecture with carbonized outer surface. (c) HRTEM image of ZHC with disordered structure. (d-h) EDS mapping of ZHC.
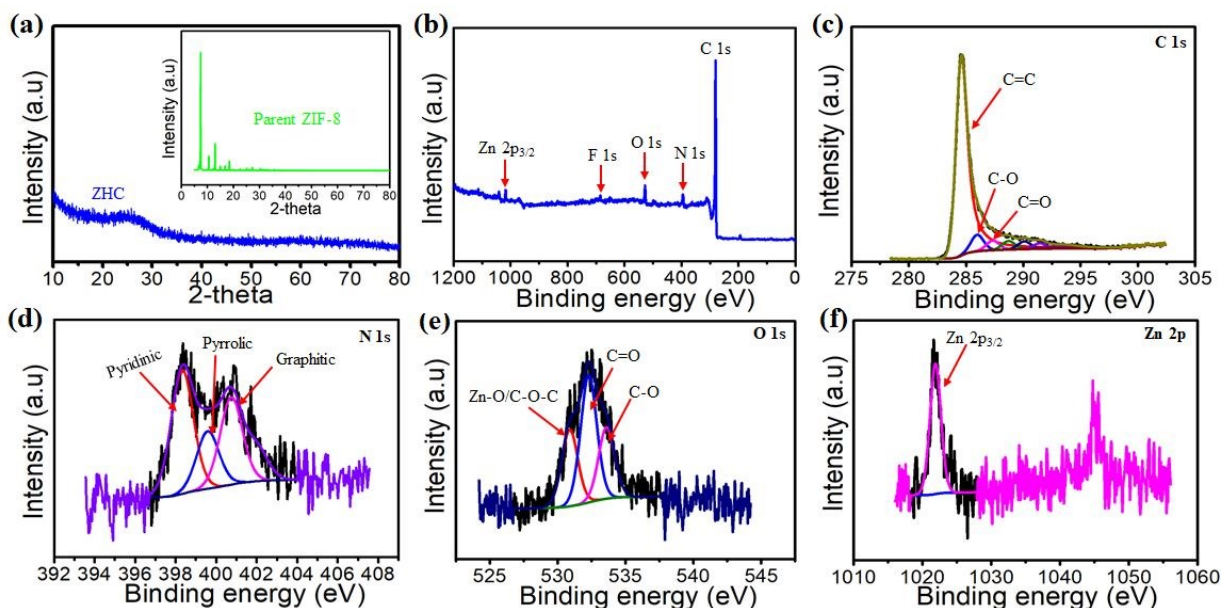
Figure 3. (a) XRD patterns for ZHC and parent ZIF-8. (b) XPS survey of ZHC with deconvolution of (c) carbon, (d) nitrogen, (e) oxygen and (f) zinc.

Realizing the favourable advantages of ZHC to control over PSs, the ZHC coated Celgard PP separator was implemented for LSB fabrication. The cycling performances of ZHC in comparison to the ZIF-8 coated Celgard is presented in **Figure 4a** in addition with the rate dependent

charge/discharge profiles and voltage profiles in **Figure 4b-d**. The ZHC coating enables initial specific capacity of 842 mAh g^{-1} (4.80 mg cm^{-2}) at 0.2 C and retained to 568 mAh g^{-1} after 400 cycles. On the other hand, the parent ZIF-8 exhibited an initial S.cap of 700 mAh g^{-1} (4 mg cm^{-2}) and retained to 331

mAh g^{-1} with a considerable decay. The enhanced capacity retention of ZHC coating confirmed that PSs diffusion problems were well addressed by the Lewis acidic Zn and polar N with strong PSs interactions and long-term cycling to the electro-catalytic effects. Moreover, the hollow carbon sphere acted as a PSs accommodator, which establishes a chemically interactive barrier against PSs diffusion across the separator, resulting in better electrochemical performance. The rate dependent performance of the battery is presented in **Figure 4b**, where the ZHC coating can withstand up to 3 C

rate and retain to 1 C with a relatively similar S.cap. The charge/discharge profiles are shown in **Figure 4c** with their respective average voltage losses in the Figure 4d. The Figure 4d shows the average voltage losses during charge/discharge, respectively, which is shown in Figure 4c. The lowest voltage loss was achieved to be ~300 mV and highest to be ~350 mV at 0.2 C and 3 C, respectively. The cycling behaviour of ZHC contained LSBs was evaluated by the CV curve at a scan rate of 0.2 and 0.25 mV S^{-1}. **Figure S4** exhibits that the LSBs shows two distinct peaks located around 2.3 V (A) and 1.7 V (B) which are respectively denoted to the formation of higher order PSs (Li$_2$Sx, x ≥ 4) and (Li$_2$S$_2$/Li$_2$S). The well-defined anodic peak at 2.50 V (C) is associated with the conversion from insoluble Li$_2$S$_2$/Li$_2$S to soluble Li$_2$Sx and eventually oxidation to the S$_8$ [27]. The diffusion rate of ions (D$_{Li+}$) were calculated using the Randles–Sevick equation to be 4.70×10^{-6} (A), 6.15×10^{-6} (B) and 5.81×10^{-6} cm^{2}s^{-1} (C) [28] (**Figure S4a-b**). The high D$_{Li+}$ indicates the higher electrocatalytic behaviour of ZHC coating to accelerate the electrochemical reactions in LSBs.
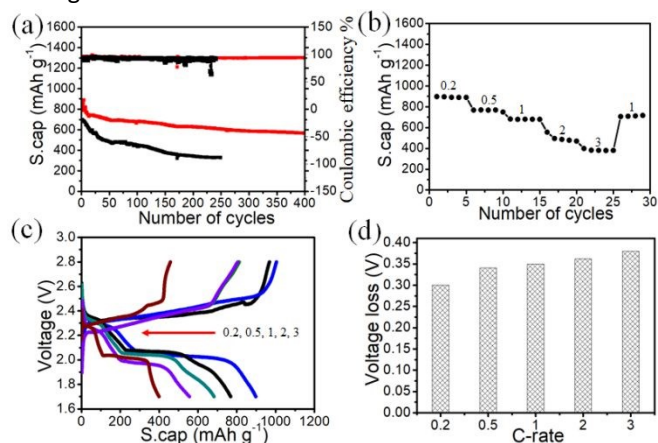
Figure 4. (a) Cycling performance of parent ZIF-8 (black) and ZHC coated Celgard (red) contained LSBs at 0.2 C. (b & c) rate performance and charge/discharge profiles of ZHC. (d) voltage losses between average charge/discharge at different c-rate is shown in (c).

The reason behind the superior electrochemical performances of ZHC over the parent ZIF-8 is further illustrated conceptually in the **Figure 1e-f**. In the presence of pristine ZIF-8 coated Celgard PP, the PSs are diffused through the coating layer due to the high porosity and react with the anode. The PSs which do not return to the cathode during cycling is lost in the LSB resulting higher S.cap loss and short life cycles. This phenomenon can be observed in the poor cycling performance shown in **Figure 4a**, where the ZIF-8 coated Celgard PP is limited to a low S.cap with only 250 cycles. However, after ZHC coating on top of the Celgard PP, the PSs diffusion through the coating is well controlled due to the chemical interactive Zn and N and the associated hollow carbon spheres.

The chemical interactions of Zn and N is also confirmed through the DFT analysis as shown in **Figure S6**. The adsorption energies were calculated to be -1.57, -2.93 and -3.53 as per Li$_2$S, Li$_2$S$_2$ and Li$_2$S$_8$, respectively. The DFT analysis proves that the Zn and N has a strong affinity with the PSs as the adsorption energy is higher than conventional carbon-based materials (0.1-0.7 eV). The dual impact of the chemical interactions and the hollow sphere structure are identified to be beneficial to enhance the electrochemical performance of the ZNF over the parent ZIF-8 MOF.

The surface morphology of the anodes for both ZIF-8 and ZHC is a good indication of successful shuttle mitigation in LSBs. As such, the LSBs for both ZIF-8 and ZHC were dismantled and SEM analysis was carried out to see the surface modifications. Both ZIF-8 and ZHC modified anode surfaces (**Figure 5b-c**) are modified after cycling in comparison to the pristine anode (**Figure 5a**). However, the anode surface from the ZHC LSB is smoother in comparison to the anode surface from the ZIF-8 LSB indicating more defensive nature of ZHC to control the PS diffusion. Furthermore, the low intensity sulfur peak in the EDS spectra is another indication that the ZHC provides a better defence to the PS shuttle in LSBs. **Figure 5f** shows the cross section of the ZHC coating on the Celgard PP separator after cycling. The layer is still strongly adhered to the separator and there is a presence of sulfur in the EDS. A visualization test was employed to directly describe the interaction of ZHC with the PSs (**Figure 5g**) where the ZHC coating shows a very slow diffusion of PSs over time. To screen out this process, a small bottle containing a 0.5 M Li$_2$S$_8$ solution was capped with the ZHC coated Celgard PP which was separated by a larger bottle with 2 mL of electrolyte.
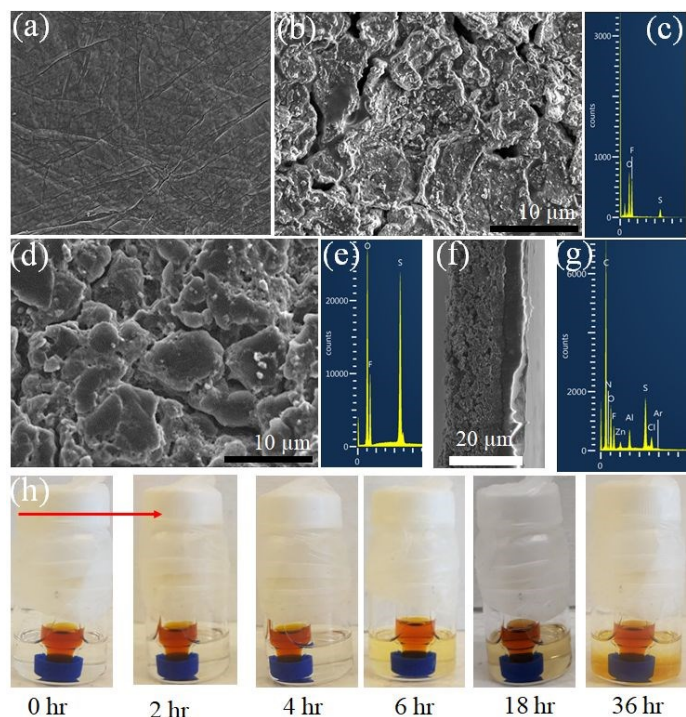
Figure 5. (a) Pristine anode. (b-c) Cycled anode for ZHC with its EDS mapping shown in (c). (d) Cycled anode for ZIF-8 with its EDS mapping shown in (e). (f) Cross section of cycled ZHC coated (thickness 20 μm) Celgard PP with its EDS mapping shown in (g). (h) PSs diffusion test through ZHC coated Celagrd PP into the electrolyte.

Conclusion

The ZHC coating has been successfully implemented to defend the PS diffusion in LSBs. The ZHC coating has confirmed better specific capacity, good cycling stability at higher rates as compared to the pristine ZIF-8. The superior electrochemical performance of ZHC can be pointed to the following advantages: (i) Hollow sphere of ZHC acted as an PSs accommodator to capture huge volume change during electrochemical reactions to avoid capacity fading and control the shuttle effect. (ii) Microporous architecture has been beneficial to physical prohibition of PSs. (iii) The conductive outer surface layer allowed easy access to electron and ions during cycling to promote the electrochemical performance. (iv) Zn and N have shown strong chemical interactions with the PSs to limit the PS diffusion. (v) The ZHC is lightweight which is beneficial to fabricate compact LSBs with high energy density. Finally, the ZHC based LSBs with good electrochemical performance is attractive to provide new insight to design the LSBs with high sulfur loading.

Experimental section

Preparation of hollow ZIF-8-derived hollow carbon (ZHC):

The ZIF-8 was synthesized from zinc acetate (Zn $(CH_3COO)_2\cdot 2H_2O$) and 2-methylimidazole ($C_4H_6N_2$) aqueous solutions. In details, 200 mL of Zn precursor solution (aq) was prepared using 20.0 g of Zn $(CH_3COO)_2\cdot 2H_2O$. To make organic linker solution, 40.0 g of the $C_4H_6N_2$ was dissolved in 200 mL of deionized water (DIW). After preparation of each clear reaction solutions, they were mixed and the reaction solution was stirred at room temperature (R.T.) for 30 min and kept overnight. The ZIF-8 powder was collected by centrifugation at 7000 rpm and washed several times with ethanol and DIW to remove residue. This washing process was checked with pH-indicator paper. Final product was dried at 60 °C in convection oven for 24 hours, then, the white powder was dried at 60 °C under vacuum. The 1 g of synthesized ZIF-8 was dispersed in 50 mL of DIW by sonication to make ZIF-8 solution. The etching solution (aq) was prepared by 5 g of tannic acid and 50 mL of DIW. Two solutions were mixed and stirred for 5 hr. The resulted yellowish-brown colored solution was centrifuged at 7000 rpm and washed several times with water and ethanol to get the hollow ZIF-8 powder. After washing process, the resulted product was dried in oven. Then, the hollow ZIF-8 powder was kept under Ar for 30 min in the furnace before increasing the temperature. Then, the temperature was increased up to 800 °C with a heating rate of 5 °C/min and kept for 3 hours under Ar flow. Hollow ZIF-8 was successfully converted into nanoporous hollow carbon (ZHC).

Preparation of Sulfur Electrode and Electrolyte

The sulfur/carbon composite was prepared using the melt diffusion method. In this method, carbon nanotubes (CNTs)/sulfur composite having 70 wt % sulfur designated as CNT-70 was prepared through the melt diffusion method at 155 ° C. The 80 wt % of CNT-70 was mixed with conductive additive Super P (10 wt %) and PVDF binder (10 wt %) to make a slurry for the electrode preparation. Finally, this slurry was pasted on the top of a carbon coated aluminium foil by slurry coating doctor blade. The slurry coated aluminium foil was dried in a vacuum oven at 60 °C for 12 hours and cut into circular discs with a diameter of 10 mm.

The electrolyte solution was prepared using a 1,3 dioxolane (DOL) and 1,2 dimethoxymethane (DME) at the volumetric ratio of 1:1, 1 M lithium bis (trifluoromethanesulfonyl) imide (LiTFSI) and 0.1 M LiNO_3. The electrolyte was prepared inside a glovebox, supplied with Ar, with O_2 and H_2O levels below 0.1 ppm to avoid air and moisture contamination.

Preparation of ZHC coated Celgard PP

The ZHC materials was ultrasonically dispersed in NMP (N-Methyl 2-pyrrolidone) and PVDF (Polyvinylidene fluoride) for 20 minutes followed by a simple vacuum filtration of the suspension through the commercial Celgard PP separator. The obtained ZHC/PP separator was dried at 60 °C in a vacuum oven for 12 hours and cut into 16 mm diameter to be used for LSB application.

Battery Assembly

The LSBs were fabricated inside an Ar-filled glove box at 0.1 ppm of H_2O and O_2 pressure. A lean electrolyte/sulfur ratio of 7 µL/mg was considered to assemble the LSBs. A hydraulic crimping machine (MSK-110 Crimper) was used to seal the LSBs for electrochemical testing.

Electrochemical Measurements

The LAND system was used to acquire the electrochemical performance of LSBs within a voltage window of 1.7-2.8 V (Li/Li^+). The Biologic VSP also was used to capture the CV profiles of the inactivated and activated cells at 0.2, 0.25 mV s^{-1}, respectively.

Characterizations tools

The morphology and structure of the ZIF-8 and ZHC samples were characterized using a field emission transmission electron microscopy (FE-TEM F20) and a scanning electron microscope (SEM) (SU-3500). The SU-3500 is equipped with an Oxford X-MAXN energy-dispersive X-ray spectroscopy (EDS) detector.

The XRD (X-ray diffraction) of samples were analysed on a Bruker D8 Advance Powder X-ray diffractometer equipped with a Cu source, operated at 40kV and 40mA, and an energy discriminating 2D array detector that minimises a fluourescent background. Data were collected using a Bragg-Brentano geometry with a 0.12-degree divergence slit from 5 degrees to 80 degrees two-theta at a resolution of 0.02 degree and at 1.2 second per step

X-ray photoelectron spectroscopy (XPS) survey data was acquired using a Kratos Axis ULTRA XPS incorporating a 165 mm hemispherical electron energy analyser. The incident radiation was monochromatic Al Kα X-rays (1486.6 eV) at 150 W (15 kV, 10 mA). Survey (wide) scans were taken at an analyser pass energy of 160 eV and multiplex (narrow) high resolution scans at 20 eV. Survey scans were carried out over 1200-0 eV binding energy range with 1.0 eV steps and a dwell time of 100 ms. Narrow high-resolution scans were run with 0.05 eV steps and at a dwell time of 250 ms. The base pressure in the analysis chamber was 1.0 x10^{-9} torr and

during sample analysis 1.0 x 10^{-8} torr. Atomic concentrations were calculated using the CasaXPS version 2.3.14 software and a Shirley baseline with Kratos library relative sensitivity factors (RSFs). Peak fitting of the high-resolution data was also carried out using the CasaXPS software.

N_2 adsorption-desorption isotherms were measured using a Tristar II (Micromeritics Vac prep-061). The surface area and the pore size distribution of the samples were measured by Brunauer-Emmett-Teller (BET) method and non-local density functional theory (NLDFT) methods, respectively. Thermal gravimetric analysis (Perkin Elmer, Diamond TG) (TGA) for CNT-70 was performed in nitrogen atmosphere to measure weight % mass loss at a heating rate of 10°C min^{-1} till 800 °C.

Author Contributions

All authors have contributed for this research.

Conflicts of interest

"There are no conflicts to declare".

Acknowledgements

References

1.   M. Rana, S. A. Ahad, M. Li, B. Luo, L. Wang, I. Gentle and R. Knibbe, *Energy Storage Materials*, 2019, **18**, 289-310.
2.   M. Rana, M. Li, X. Huang, B. Luo, I. Gentle and R. Knibbe, *Journal of Materials Chemistry A*, 2019, **7**, 6596-6615.
3.   W. Ren, W. Ma, S. Zhang and B. Tang, *Energy Storage Materials*, 2019, **23**, 707-732.
4.   Y. Yang, G. Zheng, S. Misra, J. Nelson, M. F. Toney and Y. Cui, *Journal of the American Chemical Society*, 2012, **134**, 15387-15394.
5.   Q. Pang, X. Liang, C. Y. Kwok and L. F. Nazar, *Nature Energy*, 2016, **1**, 16132.
6.   Y.-S. Su and A. Manthiram, *Nature communications*, 2012, **3**, 1166.

Nanoscale Accepted Manuscript

7. M. Rana, Q. He, B. Luo, T. Lin, L. Ran, M. Li, I. Gentle and R. Knibbe, *ACS central science*, 2019, **5**, 1946-1958.

8. J. Zheng, J. Tian, D. Wu, M. Gu, W. Xu, C. Wang, F. Gao, M. H. Engelhard, J.-G. Zhang and J. Liu, *Nano letters*, 2014, **14**, 2345-2352.

9. M. Liu, F. Ye, W. Li, H. Li and Y. Zhang, *Nano Research*, 2016, **9**, 94-116.

10. J. Xu, T. Lawson, H. Fan, D. Su and G. Wang, *Advanced Energy Materials*, 2018, **8**, 1702607.

11. M. Rana, B. Luo, M. R. Kaiser, I. Gentle and R. Knibbe, *Journal of Energy Chemistry*, 2020, **42**, 195-209.

12. A. Fu, C. Wang, F. Pei, J. Cui, X. Fang and N. Zheng, *Small*, 2019, **15**, 1804786.

13. D. Lin, Y. Liu and Y. Cui, *Nature nanotechnology*, 2017, **12**, 194.

14. M. M. Rana, J. Kim, L. Peng, H. Lim, R. Kaiser, L. Ran, B. Luo, Z. Han, M. S. A. Hossain and X. Lu, *ACS Applied Energy Materials*, 2020.

15. Z. Wang, L. Zhou and X. W. Lou, *Advanced materials*, 2012, **24**, 1903-1911.

16. M. H. Oh, T. Yu, S.-H. Yu, B. Lim, K.-T. Ko, M.-G. Willinger, D.-H. Seo, B. H. Kim, M. G. Cho and J.-H. Park, *Science*, 2013, **340**, 964-968.

17. Q. Zhang, T. Zhang, J. Ge and Y. Yin, *Nano letters*, 2008, **8**, 2867-2871.

18. C. Avci, J. Ariñez-Soriano, A. Carné-Sánchez, V. Guillerm, C. Carbonell, I. Imaz and D. Maspoch, *Angewandte Chemie*, 2015, **127**, 14625-14629.

19. Z. X. Cai, Z. L. Wang, J. Kim and Y. Yamauchi, *Advanced Materials*, 2019, **31**, 1804903.

20. A. Singer, Z. Barakat, S. Mohapatra and S. S. Mohapatra, in *Nanocarriers for Drug Delivery*, Elsevier, 2019, pp. 395-419.

21. Y.-S. Su and A. Manthiram, *Nature communications*, 2012, **3**, 1-6.

22. D. Saliba, M. Ammar, M. Rammal, M. Al-Ghoul and M. Hmadeh, *Journal of the American Chemical Society*, 2018, **140**, 1812-1823.

23. W. Zhang, X. Jiang, Y. Zhao, A. Carné-Sánchez, V. Malgras, J. Kim, J. H. Kim, S. Wang, J. Liu and J.-S. Jiang, *Chemical science*, 2017, **8**, 3538-3546.

24. M. Rana, J. Kim, L. Peng, H. Lim, R. Kaiser, L. Ran, B. Luo, Z. Han, M. Hossain and X. Lu, *ACS Applied Energy Materials*, 2020.

25. P. Chiochan, S. Kaewruang, N. Phattharasupakun, J. Wutthiprom, T. Maihom, J. Limtrakul, S. S. Nagarkar, S. Horike and M. Sawangphruk, *Scientific reports*, 2017, **7**, 1-10.

26. Y. Qiu, W. Li, W. Zhao, G. Li, Y. Hou, M. Liu, L. Zhou, F. Ye, H. Li and Z. Wei, *Nano letters*, 2014, **14**, 4821-4827.

27. M. Xiang, H. Wu, H. Liu, J. Huang, Y. Zheng, L. Yang, P. Jing, Y. Zhang, S. Dou and H. Liu, *Advanced Functional Materials*, 2017, **27**, 1702573.

28. X. Huang, K. Zhang, B. Luo, H. Hu, D. Sun, S. Wang, Y. Hu, T. Lin, Z. Jia and L. Wang, *Small*, 2019, **15**, 1804578.